Chemical Science

Accepted Manuscript

This article can be cited before page numbers have been issued, to do this please use: A. Ogunleke, B. Recur, H. Balacey, H. Chen, M. Delugin, Y. Hwu, S. Javerzat and C. Petibois, *Chem. Sci.*, 2017, DOI: 10.1039/C7SC03306K.

ROYAL SOCIETY OF CHEMISTRY

rsc.li/chemical-science

View Article Online
DOI: 10.1039/C7SC03306K

3D chemical imaging of the brain by quantitative IR spectro-microscopy

Abiodun Ogunleke[1], Benoit Recur[1], Hugo Balacey[1], Hsiang-Hsin Chen[2], Maylis Delugin[1], Yeukuang Hwu[2], Sophie Javerzat[1], Cyril Petibois[1,2]

Affiliations:
1: University of Bordeaux, Inserm U1029 LAMC, Allée Geoffroy Saint-Hilaire Bat. B2, F33600 Pessac, France
2: Academia Sinica, Institute of Physics, 128 Sec. 2, Academia Rd., Nankang, Taipei 11529, Taiwan R.O.C.

Abstract:
Three-dimensional (3D) histology is the next frontier for modern anatomo-pathology. Characterizing abnormal parameters in a tissue is essential to understand the rationale of pathology development. However, there is no analytical technique, *in vivo* or histological, able to discover such abnormal features and provide their 3D distribution at microscopic resolution. Here, we introduce a unique high-throughput infrared (IR) microscopy method, which combines automated image corrections and subsequent spectral data analysis for 3D-IR image reconstruction. We performed the spectral analysis of a complete organ for a small animal model, a mouse brain with an implanted glioma tumor. The 3D-IR image is reconstructed from 370 consecutive tissue sections and corrected with the X-ray tomogram of the organ for an accurate quantitative analysis of chemical contents. A 3D matrix of 89.10^6 IR spectra is generated, allowing to separate the tumor mass from healthy brain tissues based on various anatomical, chemical, and metabolic parameters. We demonstrate that quantitative metabolic parameters can be extracted from IR spectra for characterization of brain vs. tumor metabolism (assessing the Warburg effect in tumor). Our method can be further exploited by searching for whole spectral profile discriminating tumor vs. healthy tissue in a non-supervised manner, which we call 'spectromics'.

Keywords
3D chemical imaging, IR microscopy, histology, brain, cancer

Introduction

Three-dimensional (3D) microscopy is a powerful approach to image biological specimens[1]. It offers excellent spatial resolution and facilitates observation of tissue sub-structures and contents[2] under physiological and pathological conditions. However, although it is feasible to achieve high spatial resolution close to the diffraction limit in small, transparent biological specimens[3], such as cultured cells, it remains difficult to achieve high-resolution images of larger, more optically challenging entities such as tissue blocks, biopsies, or organs[4]. 3D pathology is expected because tissue blocks are not naturally transparent, contain complex 3D networks (blood and lymph systems, membranes, nerves and other fibers, etc.), a 3D arrangement of different cell phenotypes that is not homogeneous neither, and an extracellular space that is composed of many other compounds and filamentous structures. From a geometric volume, it is in principle possible to instantly visualize tissue abnormalities, with significant advantages compared to the usual 2D histology[5]. However, labeling techniques are not quantitative approaches, therefore 3D rendering can't provide the distribution of molecular concentrations[4]. Accessing to molecular concentrations will be crucial to overcome the current interpretation limit of pathological features, based mostly on anatomical rendering.

Several approaches have already been proposed for *ex vivo* 3D spectro-microscopy imaging, such as serial sections based electron[6], x-ray fluorescence[7], infrared[2,8], mass[9], and Raman[10] microscopies, with a 3D reconstruction of small tissue volumes at the micro- and nano-scopic scales. Mass spectrometry (MS) imaging has been the first spectroscopy technique able to propose a 3D reconstruction of a tissue' chemical information[11]. In principle, mass spectra can provide thousands of signals recorded from each voxel of the 3D MS image. A wide variety of molecules can be imaged in this way, including proteins, peptides, lipids, and endogenous and exogenous metabolites, although not all together. Thus, no global chemical information can be obtained from the sample (namely, including proteins, lipids and sugars).

A common limit to all chemical imaging techniques that might be used for 3D volume rendering is that, at microscopic scale, the 3D reconstruction is considerably more challenging relative to two-dimensional imaging

View Article Online
DOI: 10.1039/C7SC03306K

because sectioning artifacts such as tissue tears, bends, folds, and cracks become unmanageable[12]. Moreover, in 3D pathology, it is also mandatory to consider the soft tissue distortions due to the organ removal by surgery or biopsy. The shape of the tissue is considerably altered by cryomicrotomy and the final 3D reconstruction model from serial 2D sections will be significantly distant from the reality. For quantitative analyses in 3D pathology, the determination of molecular concentrations as well as the distribution of tissue sub-structures will be directly dependent on the recovery of the tissue/organ native 3D shape[13]. As a general consideration, the lack of 3D image of the tissue/organ in its native shape is a major methodological issue for histological analyses, in 2D and in 3D. To overcome that limitation in the development of 3D pathology methods, MRI[14], μ-CT[13], and ultrasound[15] *in vivo* imaging have been used to provide the actual volume of the tissue to analyze.

Here, we present an analytical methodology for developing 3D quantitative pathology. Our experimental strategy is based on a combination of X-ray **tomography** for the *in vivo* acquisition of the 3D image of the mouse brain in the skull with infrared (IR) spectro-microscopy for the histological analysis. The results shown in this paper are obtained on a mouse brain in which glioma tumor cells had been implanted to grow a tumor in 28 days before acquisition of 3D *in situ* and 2D histological images. The presence of a tumor in the brain was the perfect challenge for a quantitative chemical analysis of tissues: tumors are highly different from healthy tissues in terms of chemical composition [16] and metabolism[17].

Results and discussion:

1- Acquisition of the actual 3D shape of the brain

We first used mice heads for X-ray tomographic analysis of the brain volume (video in Supplementary material 1). Heads were analyzed with and without brain inside the skull to obtain the actual brain volume by subtraction of segmented 3D images. The segmentation method allowed to obtain the meshing of brain with a 2-μm accuracy (figures and videos in Supplementary materials 2 and 3). The high-resolution images were used as models for resizing the low-dose 3-projections X-ray images. The objective was to obtain a 3D image of the brain without altering its contents due to ionizing radiations, but at the same time, the choice of X-ray microscopy was also to avoid the use of contrast agents or labeling methods (as for MRI[18], PET/SPECT[19], intravital imaging[20], etc.), which modify the chemical contents of the sample. It would have thus affected the chemical analyses by IR microscopy after histology. The volume rendering from 3 axial absorption projections allowed to obtain a realistic volume rendering of the mouse brain that was used to virtualize all tissue sections and create a 2D mask of their planar limits. The main issue following the acquisition of a brain volume from 3 axial absorption projections was to determine the start and end points of brain sectioning as well as the actual axis of sectioning. This issue was solved by using an available anatomical atlas of the mouse brain, the Allen Mouse Brain Atlas[21,22] (Supplementary material 4). We resized the atlas with respect to the actual volume of the mouse brain. To this end, a graph-theoretic slice-to-slice reconstruction was performed with a global histology-to-CT reconstruction to achieve high accuracy, both in the alignment of features between slices and in the 3D shape of the reconstructed brain.

Methods have been proposed for a 3D reconstruction of tissue blocks, but these ones were first stained[23] or used block-face photographic volume registration[5] with MRI to help correct the shape of soft tissue images. But still, the use of labeling and staining methods or gadolinium injections for MRI prevent further "unaltered" chemical analysis. Our methodology overcome such bottleneck, providing both an image registration and correction method for reconstructing 3D tissue blocks, and achieving to determine molecular concentrations in 3D at microscopic resolution. The key advantage is the development of a genuine combination of *in vivo* 3D imaging with quantitative spectro-microscopy for producing a 3D quantitative chemical image of a tissue block. Our technique requires only a fresh-frozen tissue block to obtain a 3D chemical image.

2- Acquisition of a 3D IR spectrum matrix of the brain

After acquisition of the three X-ray projections for volume rendering of the brain, the organ was removed from skull and deposited in the upright position (with cerebellum on the bottom – thus tamping the brain volume in the coronal axis) on sample holder for continuous transverse cryomicrotomy at a 20-μm thickness. A series of 340-385 sections could be obtained depending on the organ size. Alternately, one section was stored for conventional histology (named histological images) and one section was processed for IR microscopy analysis

View Article Online
DOI: 10.1039/C7SC03306K

(named IR images). The goal was to obtain a series of histological sections sufficiently representative of the whole brain for comparative analyses between IR microscopy and histology, and for 3D image reconstructions. An example of 2D IR image of the mouse brain with typical IR spectra from different anatomical regions is shown in Supplementary material 5.

IR spectra from different regions of the brain show very different absorption profile, thus confirming that variations of chemical contents are significant. For individual 2D-IR images, the $\int(1800\text{-}900\ cm^{-1})$ intensity scale ranged 0-192 to 0-331 for the whole set of 185 images. The intensity scale was set free for the 3D-IR image reconstruction. The first reconstruction of the 3D-IR image from 2D raw IR images (without any planar shape correction) was center-aligned using the central axis between lobes as anatomical reference. As shown in figure 2, the general shape of the 3D-IR image of the brain contained numerous distortions. They came from organ shape alterations during surgery (due to the relapse of the brain volume once extracted from the skull, which exerts a pressure on brain tissues, and also due to the gravity-related collapse of this very soft tissue at deposition on the sample holder). This was also due to the well-known tissue alterations during cryomicrotomy, where tears, bends, cracks, etc. appear at the tissue sectioning or deposition process. This is showing clearly the relevance of using a 3D *in situ* (or *in vivo*) imaging method for obtaining a realistic volume rendering of the mouse brain before histological analyses. This is also a critical to ensure further quantitative chemical analysis from the 3D-IR image.

3- Correction of the 2D histological images from 3D X-ray tomogram

The IR and histological images were corrected for shape alterations using the X-ray tomogram and the 100 virtual slices (from 100 images - figure 1) given by the Allen Mouse Brain Atlas. We first compared anatomical images with the IR and histological images to define the sectioning plan effectively used while obtaining all histological sections. The anatomical images are resized according to the actual 3D volume of the mouse brain. They serve as global reference for comparing anatomical regions observed from visible, histological, and IR images. Importantly, they allow defining the first and last sections obtained on a mouse brain by cryomicrotomy, which number is variable according to the size of the organ and some potential loss of sections at extremities. They are also used for proper alignment and 3D patching after shape corrections, as shown in figure 1.

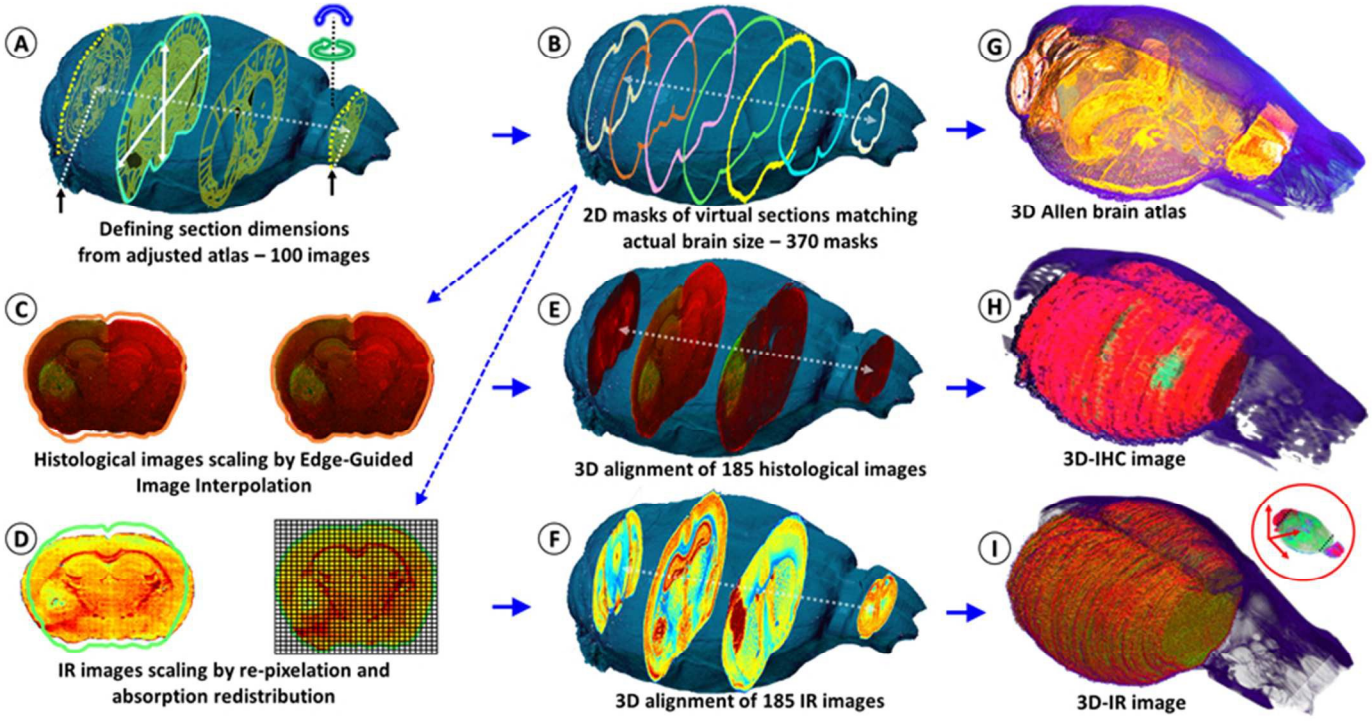

Figure 1: Schematic of the shape corrections process for 2D Images and 3D volume reconstructions. The actual volume model of the mouse brain is used to resize the anatomical images of the Allen Mouse Brain Atlas in

View Article Online
DOI: 10.1039/C7SC03306K

(A). The first and last frames corresponded to the limits of the full set of tissue sections obtained by continuous cryomicrotomy (histological and IR – 370 sections). In (B), the virtual 2D masks of the 370 images are extracted from the actual volume of the mouse brain. (C): Histological images are corrected by edge-guided image interpolation. (D): The IR images are corrected by re-pixelation and redistribution of the full spectral absorbance. The total spectral absorbance of the 2D IR image is calculated before and after IR spectra redistribution for validation of the image correction process. (E): The 185 histological images are positioned in the actual volume model of the mouse brain for 3D alignment and patching. The alignment of each IHC image is performed by a global smoothed slice-shape morphing with a normalized redistribution of pixel values over the reached virtual slice surface (extracted from the X-ray model 2D-mask). (F): The 185 IR images are also aligned and patched according to the same procedure. (G-I): 3D reconstructions of the Allen brain atlas, 3D-IR image and 3D-IHC image resized to match the actual dimensions of the mouse brain.

The sets of IR and corresponding histological images (370 dual images) were used for a brain volume rendering. The average deviation observed from 2D image corrections was 11% in height and 8% in width. The 3D histological image was segmented to highlight the tumor (labeled, green fluorescence – Supplementary material 6). We can observe that the reconstructed 3D images of the brain perfectly match the actual volume of the brain defined in by X-ray tomogram. We applied a classical IR spectroscopy analysis to highlight the tumor from the 3D chemical image, i.e., the protein-to-lipid ratio defined by absorption ratio $\int(1700\text{-}1480\ cm^{-1})/\int(1760\text{-}1710\ cm^{-1})$, or the absorption ratio between amide I and lipid esters[24-26]. This analysis highlights the tumor mass, containing higher concentration in proteins and lower concentration of lipids than its surrounding tissues.

4- Anatomy of the brain based on 3D chemical data

An important objective of our study was to demonstrate that 3D chemical imaging by IR spectro-microscopy can be used for the 3D pathological investigation of large tissue blocks. We segmented the tumor mass based on a simple spectral analysis to compare it with tumor volume rendering from the 3D histological image (Supplementary materials 7-8). As expected, the IR spectra extracted from the tumor and at a similar location in the left hemisphere show important differences for most of absorption regions. The shape of tumor volume was found very similar between IR and histological analyses, the calculation of Hausdorff distances[27] between the two volumes showing only marginal differences on the global shape of the tumor, but a significant difference in volume calculation (3D-IR = 9.39 mm^3; 3D-IHC = 12.24 mm^3; difference ~30%). The ability to extract the 3D spectrum matrix of the tumor mass is important to analyze specifically its chemical contents. This is also true for the healthy brain tissues (at least the left hemisphere, which is not affected by the tumor metabolism and the mechanical pressure it exerts on the surrounding tissues). The figure 2 shows examples of segmentation performed on the mouse brain 3D-IHC and 3D-IR images, both for the tumor mass extraction and for defining anatomical structures from chemical analyses on the 3D IR image. This segmentation can be based on absorption profiles extracted from spectra (as for the tumor mass with the lipid/protein contrast). It is noteworthy that healthy brain tissues and anatomical entities can be successfully separated directly from IR spectra. Therefore, an anatomical atlas of the mouse brain can be developed from its 3D quantitative chemical image.

View Article Online
DOI: 10.1039/C7SC03306K

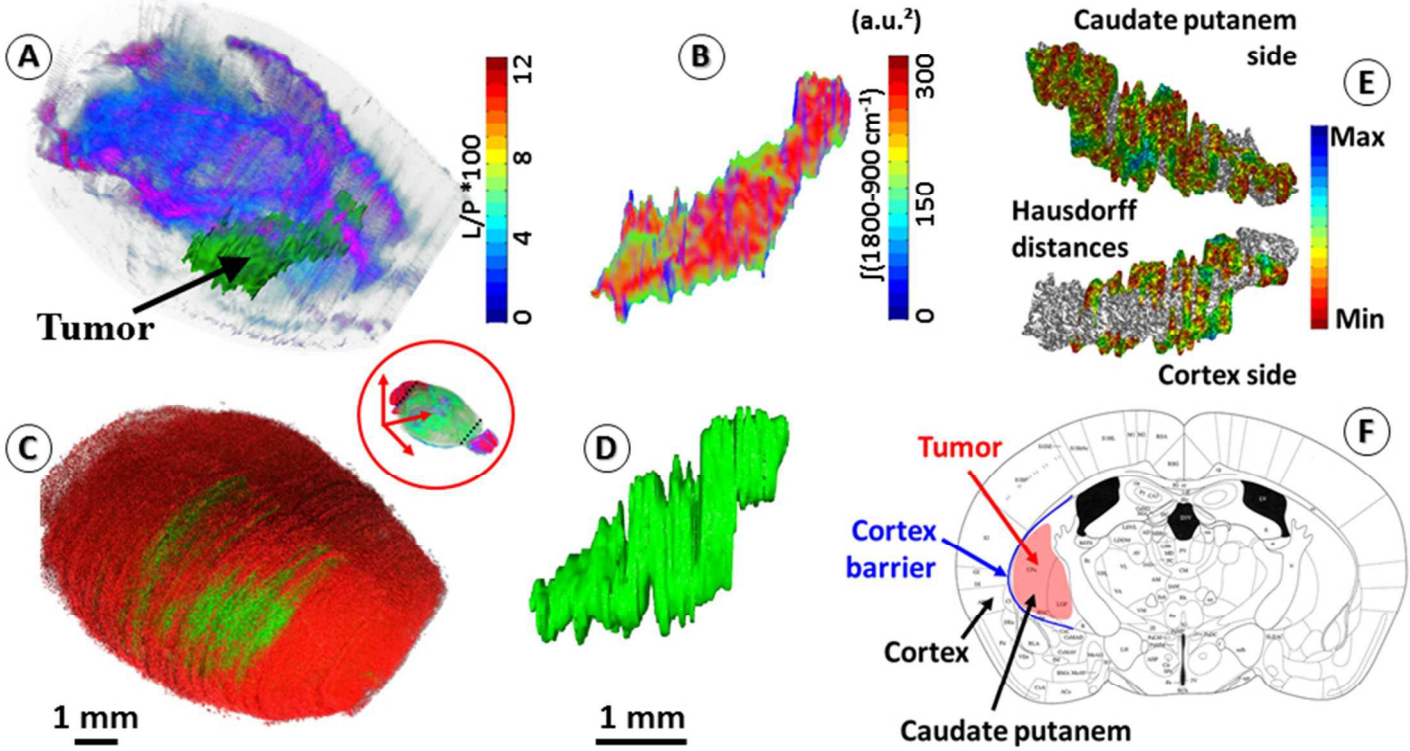

Figure 2: Segmentation of brain regions based on chemical contents. (A): 3D-IR image of the mouse brain in the skull highlighting the tumor mass using the [∫(1760-1710 cm^{-1})/∫(1700-1592 cm^{-1})*100] absorption ratio (L/P as indicated in figure scale legend – videos provided as Supplementary materials 7-8). With the tumor seen mostly in green, we can also distinct the white matter distribution as the purple-blue part of the brain image. (B): 3D-IR image of the tumor mass extracted from whole brain by segmentation of the voxels presenting the chemical profile of the tumor (full spectral absorbance). (C-D): similar views of tumor mass in the skull and extracted from the 3D-histological image (green channel segmentation for the tumor). (E): Representation of the Hausdorff distances between the 3D-histology (reference) image of the tumor mass and its 3D-IR counterpart (both sides of the tumor mass). (F): Illustration of the tumor growth mechanics as revealed by the segmentation of 3D-IHC and 3D-IR images of the tumor volume with respect to the brain regions invaded.

The distinction between white and gray matter is similar to previous studies[28]. The Hausdorff distance calculation reveals further interesting features (Supplementary material 8). The 3D-IHC image of the tumor is showing the tissue volume occupied by tumor cells. Conversely, the 3D-IR image is showing the tissue volume which chemistry is significantly altered by tumor cells. The 30% difference between the two volumes represents the tissue volume where tumor cells are present in 3D-IHC image but where they did not alter yet significantly the chemical composition of the tissue, as revealed by the 3D-IR image[24]. Thus, the difference is related to tissue areas where tumor cells are dispersed. On the tumor side in front of the cortex, the differences between IHC and IR images are very limited because the tumor is massive. Therefore, the tumor was blocked by the cortex barrier (except along the "tunnel" formed by the needle when implanting the tumor cells). On the opposite side, the differences between IHC and IR images are more significant because the tumor is more diffuse. This is showing that the tumor had easier way to invade the parenchyma through the caudate putamen region. This result illustrates the importance of 3D histology for understanding the anatomical-mechanical-chemical features that drive the growth of a tumor.

5- Quantitative 3D metabolic images based on 3D chemical data

The last major objective of this study was to demonstrate that 3D IR spectro-microscopy can achieve a quantitative molecular analysis of tissues. With the example of a tumor, the challenge was to analyze major metabolic parameters of the brain[29], the glycogen, glucose and lactate concentrations. To obtain a quantitative analysis, we performed an absorption integration from the glucose[26,30] (1031 cm^{-1}), glycogen[31,32] (1024 and 1152 cm^{-1}), and lactate[31,33] (1127 cm^{-1}) most specific IR bands on all IR spectra of the 3D IR image of the brain

View Article Online
DOI: 10.1039/C7SC03306K

after calculating their second derivative, a standard procedure for a fast IR spectral data extraction[34]. From 2nd derivative spectra, the 3D mapping of molecular concentrations in the brain was found consistent between tissue sections and thus no major contrast aberration came to alter the visual rendering of these analyses (figure 3 and Supplementary materials 9-11).

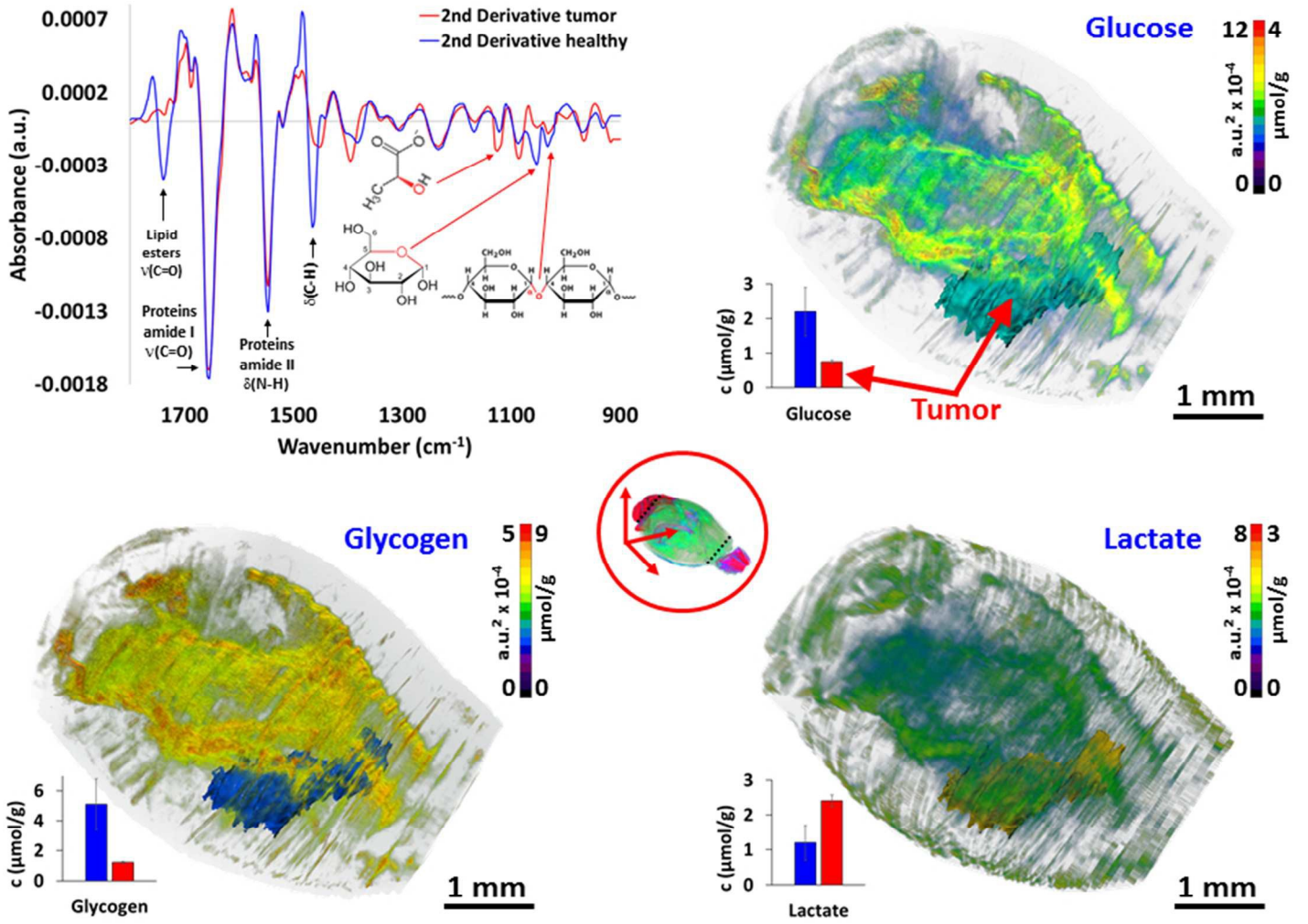

Figure 3: Quantitative metabolic analysis of the brain. From 2nd derivative of the 3D spectrum matrix, the glucose, glycogen and lactate IR absorptions are quantified and mapped for the whole brain. The 3D volume renderings with molecular concentrations have been determined according to the healthy brain (left hemisphere) as a reference (3D renderings are shown in Supplementary materials 9-11). Images are scaled with equivalent absorption (a.u.² .10^{-4}) and concentration (µmol/g) values.

We first compared the molecular concentrations between enzymatic assays and IR spectra data analyses. A group of 10 mice with similar tumor mass in the right hemisphere were sacrificed to analyze their left hemisphere. Fluorescence enzymatic assays[35] made on tissue homogenates provided a 2.2 ± 0.7 µmol/g of glucose, 5.1 ± 1.7 µmol/g of glycogen, and 1.2 ± 0.5 µmol/g of lactate. These results are consistent with other studies on mice[36-39] that have been reported from similar enzymatic assays. Interestingly, the regional distributions of glucose[36] in mice brain have been found varying with a 3-fold amplitude, and 2-fold for lactate[40] and glycogen[38,41]. Such concentration variations per brain region were also found in our 3D IR images. When we considered the distribution of absorption intensities for glucose, glycogen, and lactate IR absorptions, we observed that 95% of spectra ranged within a 2-3-fold intensity scale values. Extreme values were rejected from calculations (notably the 0 values, representing 86% of rejected spectra, probably due to noisy signal or to distorted baseline preventing the use of 2nd derivative spectra absorptions). Spectra included in this study (>95%

View Article Online
DOI: 10.1039/C7SC03306K

for each anatomical region) allowed to define a distribution of concentrations in accordance with enzymatic assays performed on brain regions, glucose scale ranging 1.3 to 3.5 µmol/g, glycogen 3.6 to 8.4 µmol/g, and lactate 0.7 to 1.9 µmol/g (basically, each metabolite has a 2-3-fold concentration variation in the brain).

These concentration variations in the mouse brain are consistent with previous studies[36,39,41], although not fully comparable since microscopic studies of metabolic concentrations in brain have never been done previously on fresh – snap-frozen only - tissues. It is also important to note that the tumor exhibited a significantly lower glucose (0.8 ± 0.1 µmol/g; $P<0.05$) and glycogen (1.2 ± 0.1 µmol/g; $P<0.05$) concentrations compared to the healthy tissue counterpart in left hemisphere (considering similar locations - Supplementary material 12), while the lactate concentration was much higher (2.4 ± 0.2 µmol/g; $P<0.05$). With respect to the healthy brain tissues, these metabolic changes in tumor mass are typical of a Warburg effect, where glycolysis is increased and thus depletes the glucose-glycogen stores and consequently raises the production of lactate as a by-product[42]. However, the distributions of metabolic concentrations in the tumor mass were found very homogeneous, which is also characteristic for that size of glioma solid tumor[43]. Importantly, we tried other resolutions (5, 10, and 50 µm), and it appeared that 5-µm thick sections did not provide reliable S/N for quantitative analyses[44]. The 10-µm resolution was not reliable for 3D image reconstruction as too many sections were lost from continuous sectioning. And the 50-µm resolution was insufficient to provide all details found at 20-µm resolution. Thus, the 20-µm resolution, todays, appears as the best compromise for a large 3D IR image reconstruction.

Till now, quantitative histology remained limited to the quantitation of objects[45] and sub-structures[46] in tissue sections, but not to its chemical contents[47]. Here, we combined an efficient anatomical rendering of the mouse brain with a quantitative chemical analysis of its contents from the same dataset. The 3D volume renderings for anatomical, chemical and metabolic contents of the mouse brain with a tumor reached an incomparable level of information for a 3D microscopy analysis. As we demonstrated for anatomical and metabolic features of a mouse brain, the exploitation of the whole spectral information, called 'spectromics', from a tissue block will expand tremendously the possible applications of this methodology.

Conclusion

We used a combination of 3D *in vivo* and histological imaging techniques to achieve a quantitative 3D chemical analysis of the mouse brain. The most amazing feature of this methodology is that it can resolve and co-register anatomical and metabolic parameters from the same dataset, without the use of any reagent of imaging contrast agent. Furthermore, the IR spectroscopy technique used is by far less complex than other spectroscopies, and direct exploitation of spectral data for producing relevant 3D anatomical, chemical and metabolic images can be achieved. Our approach includes high-fidelity 3D imaging and automated mathematical analysis performed on a whole organ, promising deep impact on biomedical knowledge research.

Acknowledgements

This study was supported by the French "Agence Nationale de la Recherche" and the Taiwanese "Ministry of Sciences and Techniques" (ANR and MOST – contract "Tecsan n°2013-001-3DXIR-Pathology"), and the Banque Publique d'Investissement (BPI – PIACISN2-GDN2015 - ImpactTumors). We thank Benjamin Petibois for assistance with preparation of the videos of Supplementary materials.

References

1 Fratini, M.; Bukreeva, I.; Campi, G.; Brun, F.; Tromba, G.; Modregger, P.; Bucci, D.; Battaglia, G.; Spano, R.; Mastrogiacomo, M.; Requardt, H.; Giove, F.; Bravin, A.; Cedola, A. *Sci Rep* 2015, **5**, 8514.
2 Bobroff, V.; Chen, H. H.; Delugin, M.; Pineau, R.; Javerzat, S.; Petibois, C. *J Biophotonics* 2017, **10**, 598-606.
3 Fernandez-Suarez, M.; Ting, A. Y. *Nat Rev Mol Cell Biol* 2008, **9**, 929-43.
4 Stille, M.; Smith, E. J.; Crum, W. R.; Modo, M. *J Neurosci Methods* 2013, **219**, 27-40.

View Article Online
DOI: 10.1039/C7SC03306K

5 Vandenberghe, M. E.; Herard, A. S.; Souedet, N.; Sadouni, E.; Santin, M. D.; Briet, D.; Carre, D.; Schulz, J.; Hantraye, P.; Chabrier, P. E.; Rooney, T.; Debeir, T.; Blanchard, V.; Pradier, L.; Dhenain, M.; Delzescaux, T. *Sci Rep* 2016, **6**, 20958.
6 Mikula, S.; Denk, W. *Nat Methods* 2015.
7 Bourassa, D.; Gleber, S. C.; Vogt, S.; Yi, H.; Will, F.; Richter, H.; Shin, C. H.; Fahrni, C. J. *Metallomics* 2014, **6**, 1648-55.
8 Wood, B. R.; Bambery, K. R.; Evans, C. J.; Quinn, M. A.; McNaughton, D. *BMC Med Imaging* 2006, **6**, 1-9.
9 Kompauer, M.; Heiles, S.; Spengler, B. *Nat Methods* 2017, **14**, 90-96.
10 Yao, S.; Chen, H. H.; Harte, E.; Ventura, G. D.; Petibois, C. *Anal Bioanal Chem* 2013, **27**, 8701-7.
11 Ye, H.; Greer, T.; Li, L. *Bioanalysis* 2011, **3**, 313-32.
12 Clarke, G. M.; Murray, M.; Holloway, C. M.; Liu, K.; Zubovits, J. T.; Yaffe, M. J. *Int J Breast Cancer* 2012, **2012**, 691205.
13 Gregor, T.; Kochová, P.; Eberlová, L.; Nedorost, L.; Prosecká, E.; Liška, V.; Mírka, H.; Kachlík, D.; Pirner, I.; Zimmermann, P.; Králíčková, A.; Králíčková, M.; Tonar, Z. In *Injury and Skeletal Biomechanics*; Intech, Ed., 2012.
14 Jones, A. R.; Overly, C. C.; Sunkin, S. M. *Nat Neurosci* 2009, **10**, 1-9.
15 Schalk, S. G.; Postema, A.; Saidov, T. A.; Demi, L.; Smeenge, M.; de la Rosette, J. J.; Wijkstra, H.; Mischi, M. *Comput Med Imaging Graph* 2016, **47**, 29-39.
16 Mourant, J. R.; Yamada, Y. R.; Carpenter, S.; Dominique, L. R.; Freyer, J. P. *Biophys J* 2003, **85**, 1938-47.
17 Keckesova, Z.; Donaher, J. L.; De Cock, J.; Freinkman, E.; Lingrell, S.; Bachovchin, D. A.; Bierie, B.; Tischler, V.; Noske, A.; Okondo, M. C.; Reinhardt, F.; Thiru, P.; Golub, T. R.; Vance, J. E.; Weinberg, R. A. *Nature* 2017, **543**, 681-686.
18 Engelhorn, T.; Eyupoglu, I. Y.; Schwarz, M. A.; Karolczak, M.; Bruenner, H.; Struffert, T.; Kalender, W.; Doerfler, A. *Neurosci Lett* 2009, **458**, 28-31.
19 Toyama, H.; Ichise, M.; Liow, J. S.; Modell, K. J.; Vines, D. C.; Esaki, T.; Cook, M.; Seidel, J.; Sokoloff, L.; Green, M. V.; Innis, R. B. *Int Congress Series* 2004, **1265**, 255-61.
20 Gleave, J. A.; Lerch, J. P.; Henkelman, R. M.; Nieman, B. J. *PLoS One* 2013, **8**, e72039.
21 Lein, E. S.; Hawrylycz, M. J.; Ao, N.; Ayres, M.; Bensinger, A.; Bernard, A.; Boe, A. F.; Boguski, M. S.; Brockway, K. S.; Byrnes, E. J.; Chen, L.; Chen, L.; Chen, T. M.; Chin, M. C.; Chong, J.; Crook, B. E.; Czaplinska, A.; Dang, C. N.; Datta, S.; Dee, N. R.; Desaki, A. L.; Desta, T.; Diep, E.; Dolbeare, T. A.; Donelan, M. J.; Dong, H. W.; Dougherty, J. G.; Duncan, B. J.; Ebbert, A. J.; Eichele, G.; Estin, L. K.; Faber, C.; Facer, B. A.; Fields, R.; Fischer, S. R.; Fliss, T. P.; Frensley, C.; Gates, S. N.; Glattfelder, K. J.; Halverson, K. R.; Hart, M. R.; Hohmann, J. G.; Howell, M. P.; Jeung, D. P.; Johnson, R. A.; Karr, P. T.; Kawal, R.; Kidney, J. M.; Knapik, R. H.; Kuan, C. L.; Lake, J. H.; Laramee, A. R.; Larsen, K. D.; Lau, C.; Lemon, T. A.; Liang, A. J.; Liu, Y.; Luong, L. T.; Michaels, J.; Morgan, J. J.; Morgan, R. J.; Mortrud, M. T.; Mosqueda, N. F.; Ng, L. L.; Ng, R.; Orta, G. J.; Overly, C. C.; Pak, T. H.; Parry, S. E.; Pathak, S. D.; Pearson, O. C.; Puchalski, R. B.; Riley, Z. L.; Rockett, H. R.; Rowland, S. A.; Royall, J. J.; Ruiz, M. J.; Sarno, N. R.; Schaffnit, K.; Shapovalova, N. V.; Sivisay, T.; Slaughterbeck, C. R.; Smith, S. C.; Smith, K. A.; Smith, B. I.; Sodt, A. J.; Stewart, N. N.; Stumpf, K. R.; Sunkin, S. M.; Sutram, M.; Tam, A.; Teemer, C. D.; Thaller, C.; Thompson, C. L.; Varnam, L. R.; Visel, A.; Whitlock, R. M.; Wohnoutka, P. E.; Wolkey, C. K.; Wong, V. Y. *Nature* 2007, **445**, 168-76.
22 Yushkevich, P. A.; Avants, B. B.; Ng, L.; Hawrylycz, M.; Burstein, P. D.; Zhang, H.; Gee, J. C. In *Biomedical Image Registration. WBIR 2006.*; Pluim, J. P. W., Likar, B., Gerritsen, F. A., Eds.; Springer: Berlin, 2004; Vol. 4057.
23 Roberts, N.; Magee, D.; Song, Y.; Brabazon, K.; Shires, M.; Crellin, D.; Orsi, N. M.; Quirke, R.; Quirke, P.; Treanor, D. *Am J Pathol* 2012, **180**, 1835-42.
24 Noreen, R.; Moenner, M.; Hwu, Y.; Petibois, C. *Biotechnol Adv* 2012, **30**, 1432-46.
25 Petibois, C.; Desbat, B. *Trends Biotechnol* 2010, **28**, 495-500.
26 Petibois, C.; Déléris, G. *Trends Biotechnol* 2006, **24**, 455-62.
27 Fyllingen, E. H.; Stensjoen, A. L.; Berntsen, E. M.; Solheim, O.; Reinertsen, I. *PLoS One* 2016, **11**, e0164891.

View Article Online
DOI: 10.1039/C7SC03306K

28 Bambery, K. R.; Schultke, E.; Wood, B. R.; Rigley MacDonald, S. T.; Ataelmannan, K.; Griebel, R. W.; Juurlink, B. H.; McNaughton, D. *Biochim Biophys Acta* 2006, **1758**, 900-7.
29 Vlashi, E.; Lagadec, C.; Vergnes, L.; Matsutani, T.; Masui, K.; Poulou, M.; Popescu, R.; Della Donna, L.; Evers, P.; Dekmezian, C.; Reue, K.; Christofk, H.; Mischel, P. S.; Pajonk, F. *Proc Natl Acad Sci U S A* 2011, **108**, 16062-7.
30 Petibois, C.; Rigalleau, V.; Melin, A. M.; Perromat, A.; Cazorla, G.; Gin, H.; Deleris, G. *Clin Chem* 1999, **45**, 1530-5.
31 Hackett, M. J.; Sylvain, N. J.; Hou, H.; Caine, S.; Alaverdashvili, M.; Pushie, M. J.; Kelly, M. E. *Anal Chem* 2016, **88**, 10949-10956.
32 Banerjee, S.; Pal, M.; Chakrabarty, J.; Petibois, C.; Paul, R. R.; Giri, A.; Chatterjee, J. *Anal Bioanal Chem* 2015, **407**, 7935-43.
33 Petibois, C.; Cazorla, G.; Cassaigne, A.; Deleris, G. *Clin Chem* 2001, **47**, 730-8.
34 Goormaghtigh, E.; Gasper, R.; Benard, A.; Goldsztein, A.; Raussens, V. *Biochim Biophys Acta* 2009, **1794**, 1332-43.
35 Gip, P.; Hagiwara, G.; Ruby, N. F.; Heller, H. C. *Am J Physiol Regul Integr Comp Physiol* 2002, **283**, R54-9.
36 Shimada, M.; Kihara, T.; Watanabe, M.; Kurimoto, K. *Neurochem Res* 1977, **2**, 595-603.
37 Swanson, R. A.; Choi, D. W. *J Cereb Blood Flow Metab* 1993, **13**, 162-9.
38 Sagar, S. M.; Sharp, F. R.; Swanson, R. A. *Brain Res* 1987, **417**, 172-4.
39 Horn, T.; Klein, J. *Neurochem Int* 2010, **57**, 940-7.
40 Takimoto, M.; Hamada, T. *J Appl Physiol (1985)* 2014, **116**, 1238-50.
41 Franken, P.; Gip, P.; Hagiwara, G.; Ruby, N. F.; Heller, H. C. *Am J Physiol Regul Integr Comp Physiol* 2003, **285**, R413-9.
42 Liberti, M. V.; Locasale, J. W. *Trends Biochem Sci* 2016, **41**, 211-8.
43 Vartanian, A.; Singh, S. K.; Agnihotri, S.; Jalali, S.; Burrell, K.; Aldape, K. D.; Zadeh, G. *Neuro Oncol* 2014, **16**, 1167-75.
44 Marcelli, A.; Cricenti, A.; Kwiatek, W. M.; Petibois, C. *Biotechnol Adv* 2013, **30**, 1390-1404.
45 Chen, H. H.; Chien, C. C.; Petibois, C.; Wang, C. L.; Chu, Y. S.; Lai, S. F.; Hua, T. E.; Chen, Y. Y.; Cai, X.; Kempson, I. M.; Hwu, Y.; Margaritondo, G. *J Nanobiotechnol* 2011, **9**.
46 Zudaire, E.; Gambardella, L.; Kurcz, C.; Vermeren, S. *PLoS One* 2011, **6**, e27385.
47 Petibois, C. *Anal Bioanal Chem* 2010, **397**, 2051-2065.
48 Drogat, B.; Bouchecareilh, M.; Petibois, C.; Déléris, G.; Chevet, E.; Bikfalvi, A.; Moenner, M. *J Cell Physiol* 2007, **212**, 463-72.
49 Meuli, R.; Hwu, Y.; Je, J. H.; Margaritondo, G. *Eur Radiol* 2004, **14**, 1550-60.

Materials and Methods:

Sample preparations

The 3D image model of the mouse brain used for 2D and 3D IR image corrections has been obtained on healthy animals (10 to 12-week-old male rag-γ2C$^{-/-}$ immunodeficient mice). The study on animals has been approved by the local ethics committee (University of Bordeaux) under the agreement n° 501305-1, and all experiments were performed in compliance with the relevant laws and institutional guidelines for animal welfare. A series of 12 animals were used for acquisition of the head 3D image after dissection. The dissection consisted in the removal of the skin, eyes, tongue, teeth, etc. as to obtain the skull and the brain sample. The X-ray tomographic images were obtained in sequence with and without the brain (360 projections over 180 degrees, providing a 2-µm resolution meshing of the brain). For skull imaging, the brain was aspirated through the occipital hole. The internal part of the skull was further cleaned from possible tissue remains by enzymatic digestion (Liberase TL, Roche ref 05401020001) for 20 minutes at 37°C. The low-dose X-ray images of the brain further used for IR analyses were obtained using 3 projections (coronal, sagittal and axial views) in same conditions than for the 360 projection images, thus limiting the x-ray dose to negligible amount (not heating the brain before

View Article Online
DOI: 10.1039/C7SC03306K

histological analyses). The aim was to reconstruct the 3D model of the brain with limited 2D projections by using the high-resolution X-ray tomographic images as references.

The mouse brains prepared for 3D histological analyses had been xenografted with NCH421K glioma tumor spheroids (proneural, stem-like cells). Briefly, primary tumor-derived NCH421K spheroids (5 spheroids of $10.^4$ cells per mouse) were implanted into the right cerebral cortex using a Hamilton syringe fitted with a needle (Hamilton, Bonaduz, Switzerland) and following the procedure already described[48]. Injections were realized in the striatum (2.2 mm on left from bregma 0 and 3 mm of depth) using Hamilton syringe. Full brains (with xenografted tumor on one lobe and healthy brain on the other lobe) were removed from sacrificed mice after 28 days of tumor growth. The sample holder with brain were inserted in a plastic tube and plunged into liquid N_2 for instant freezing. The frozen brain was deposited in the upright position (with cerebellum on the bottom) on cooled glue (polyvinyl alcohol for cryostat, -20°C) to avoid tissue embedding. The total duration from the death of animal to the complete freezing of brain was always less than two minutes, what guaranty that degradation in brain cell and tissue contents was limited. A complete sectioning of the brain was performed at 20-µm thickness (Cryostat CM1900, Leica-Microsystems, France). A total of 340-385 sections was obtained depending on the brain dimensions (and where the sectioning was stopped in the cerebellum mass). The tissue slides were maintained at -80°C before IR and IHC image acquisitions. For histological imaging, all tissue sections were incubated with antibodies against human vimentin antigens (Santa Cruz 6260) and a green fluorescent secondary antibody (goat anti-mouse 488 antibody, Interchim FP-SA4010). Imaging was carried out by using a Nikon eclipse E600 microscope.

X-ray image acquisitions

Microradiology was performed with unmonochromatized (white) synchrotron X-rays emitted at the 01-A beamline wavelength shifter of the National Synchrotron Radiation Research Center (NSRRC, Hsinchu, Taiwan). The photon energy ranged from 4 keV to 30 keV with a peak intensity at ~12 keV; the beam current was kept constant at 360 mA with the top-up operation mode all over acquisition periods. To obtain 4.59×3.43 mm images X-rays were converted into visible light using a $CdWO_4$ single crystal scintillator and then detecting the photons with an optical microscope equipped with a 1600 × 1200 pixels CCD camera (model 211, Diagnostic Instruments). We reduced the radiation dose by attenuating the X-ray beam with two 550 µm silicon wafers. The dose was 33.9 Gy per 100 ms for a specimen thickness of 1 cm placed before the sample. The sample-scintillator distance was 5 cm. We used a 2× lens in the optical microscope to obtain the desired field of view; the pixel size in the final image was 2×2 µm². A simple background flattening image filter was used for large area micro-radiology images. The conceptual details of synchrotron-based microtomography, including absorption and phase contrast, have been discussed in previous study[49]. The high-resolution tomographic images were captured with 360 angles over 180 degrees. The low resolution (and low X-ray dose) images were captured with 3 angles (coronal, sagittal and axial views) and reconstructed using the high-resolution models (Supplementary materials 1-3).

IR acquisitions for 20-µm spatial resolution imaging

We analyzed the mouse brain tissue sections by IR microscopy. The QCL-IR microscope (Spero®, DRS Daylight Solutions, CA, USA) is equipped with 4 IR lasers providing wavelengths every 4 cm^{-1} along the 1800-900 cm^{-1} spectral interval, thus 225 absorption values. The microscope is constantly purged with dry air and sample compartment is isolated from ambient air by a plastic box. The detector is a non-N_2-liquid frozen focal plane array (FPA) detector with 480x480 elements. The 20-µm pixel size was obtained after acquisition by binning 5x5 pixels. IR image acquisitions lasted up to 2 hours per section at the largest tissue section dimensions, ~6x8 mm). A total of 170-190 IR images was obtained per brain for the 3D-IR image reconstruction (same number for the corresponding histological image providing a comparison between tumor volumes). The microscope was installed in a thermally controlled room (20°C) for standardizing the ambient conditions during acquisitions over the total duration of acquisitions (2 months).

3D IR and 3D histological images reconstruction

The 2D- and 3D-IR images presented in this article come from a mouse brain with 370 sections (Supplementary materials 6-7). The 2D-IR images were obtained and represented a matrix of 9.4-million IR spectra and 250 GB

View Article Online
DOI: 10.1039/C7SC03306K

of raw data on a storage server (reduced to 10 GB after processing the 5x5 pixel binning). The same number of histological sections was further obtained. The visible images of histological sections were coupled to the 2D masks of virtual brain sections extracted from the 3D X-ray tomogram of the mouse brain for further corrections and resizing (Figure 1). The resizing of 2D-histological images was done by edge-guided image interpolation. The first and last sections obtained by cryomicrotomy are marked by black arrows in figure 1-A. The 2D-mask of each image was extracted from the actual volume of the mouse brain (respecting a 20-µm distance between 2D-masks to match the thickness of histological sections). The lacking 2D-masks (370 sections vs. 100 images in the Allen brain atlas) were completed for correction of all tissue sections. Histological images were corrected for shape alterations by edge-guided image interpolation with their corresponding 2D-mask for reference (Figure 1). The IR images were corrected by re-pixelation and redistribution of the full spectral absorbance at the 2D image level. A pixel grid at resolution of the IR image (here 20-µm lateral resolution) covers the 2D-mask that the 2D-IR image must match. The IR spectra contained in IR image pixels are redistributed in the pixel grid of the 2D-mask. The total spectral absorbance of the 2D-IR image is calculated before and after IR spectra redistribution to ensure that the chemical information of the tissue section remains unchanged. The histological images are positioned in the actual volume model of the mouse brain for 3D alignment and patching. The alignment is performed for recognition of various anatomical patterns with respect to the Allen brain atlas images in figure 1-A and the 2D-masks obtained in figure 1-B. Typical anatomical features are salient angles found at the surface of brain volume, such as the longitudinal cerebral fissure, the lobe-cerebellum interfaces, etc.). The 2D-IR images are also aligned and patched according to the same procedure as for histological images.

Brain metabolic assays

In a series of 10 mice with 18-23 days of tumor development in the right hemisphere, brains were harvested for dissection of the left hemisphere (healthy tissue). Tissues were immediately weighted and brain homogenates were obtained by sonication in 10% wt/vol of 0.1 N NaOH and 0.01% SDS and centrifuged for 15 min at 16,000 g at 4°C. The supernatant was acidified and diluted with 0.03 N HCl. Glycogen and glucose were measured by a fluorescence enzymatic assay using the amyloglucosidase method[35]. Glycogen was digested with amylo-α-1,4-α-1,6-glucosidase (AG) (Sigma). The glucose levels were determined with hexokinase and glucose-6-phosphate dehydrogenase (Sigma) through formation of NADPH from the reduction of $NADP^+$. Glucose levels obtained from samples without AG were subtracted from samples with AG to determine glycogen levels. Glycogen and glucose were expressed both as micromoles per gram of fresh brain tissue (µmol/g). The effects of SD were evaluated by t-tests. For lactate, brain homogenates (20 mg) were added to 100 µl of ice-cold 3 M perchloric acid, homogenized using a homogenizer, and then centrifuged at 1,000 g for 5 min at 4°C. The resulting supernatant was mixed with buffer containing glycine, hydrazine, and NAD and then added to LDH. The fluorescence measurements were taken at 350 nm excitation and 450 nm emission. The lactate concentration was calculated from a standard curve. For comparison with IR spectral data, statistical tests were considered significant if $P < 0.05$.

IR spectra data treatments

3D-IR image reconstruction: The $\int(1800\text{-}900\ cm^{-1})$ spectral intensity integration was calculated for all IR spectra and the 3D image was reconstructed (full spectral intensity 3D image of the brain). The full spectral intensity typically ranges between 0 and 300, and this scale was applied to all 2D-IR images before 3D reconstruction. The 3D patch of 2D-IR images was first performed with uncorrected 2D-IR images (Supplementary material 13) to show the mediocre volume rendering induced by the multiple tissue sections shape alterations due to surgery, sample deposition on sample holder, and cryomicrotomy. The same 3D patch performed with corrected 2D-IR images (Supplementary material 14) by X-ray imaging allowed to align properly each 2D-IR image according to observable external anatomical details as explained above. Therefore, although the spectra data treatments were applied on 2D-IR images, the positioning of each 2D-IR image in the 3D alignment was fixed for all volume renderings.

Tumor volume: We performed the segmentation and meshing of the tumor volume after a classical spectroscopic analysis, i.e., by calculating the protein-to-lipid absorption ratio $\int(1700\text{-}1480\ cm^{-1})/\int(1760\text{-}1710\ cm^{-1})$. The mesh of the tumor volume is extracted as an independent volumetric image for shape comparison

View Article Online
DOI: 10.1039/C7SC03306K

with its 3D-histological image (figure 2 - Supplementary material 8). The meshed tumor volumes, IR and histological, were subtracted as poly-surfaces to check the relevance at using the protein-to-lipid absorption ratio to reveal a glioma tumor in the brain. The difference between IR and histological meshed volumes was measured and expressed as a percentage of the histological (reference) volume. The difference between meshed volumes of the tumor from uncorrected and corrected 3D-IR and 3D-histological images was also calculated to show the effect of 2D image corrections on tumor volume rendering.

Quantitative metabolic analyses: Several metabolic parameters (glucose, glycogen, lactate) were quantified in 2D-IR images and the distribution of concentrations was determined (figure 3 & Supplementary materials 9-12) as follows:

1- Second derivative IR spectra were calculated for the whole 3D spectrum matrix of the mouse brain. IR spectra of the left hemisphere (healthy tissues) and for the tumor (from its meshed volume) were analyzed separately.
2- The absorptions of glucose[26,30] (1031 cm^{-1}), glycogen[31,32] (1024 and 1162 cm^{-1}), and lactate[31,33] (1127 cm^{-1}) were measured by integrating band areas on second derivative spectra (glucose: 1040-1027 cm^{-1}; glycogen: 1027-1018 and 1167-1157 cm^{-1}; lactate: 1135-1114 cm^{-1} – expressed in a.u.² x10^{-4});
3- Since there is no histological method to determine the concentration of these metabolic molecules on histological sections, the calibration of molecular concentrations was established considering the average value of their absorptions as equivalent to the values of metabolic assays on the brain homogenates obtained in parallel with another batch of 10 mice (same sex, age and experimental conditions, with a glioma tumor implanted the same day as for mice used on histological/IR experiments). The calibration was performed using only the left hemisphere part of the 2D-IR images (healthy tissues not affected by the tumor). The scaling of molecular concentrations was done according to the distribution of IR absorption for each molecular absorption (a.u.² .10^{-4} ± SD vs. µmol/g → µmol/g ± SD). The normal distribution of absorptions (mean ± 3x SD, in a.u.² .10^{-4} - data not shown) was calculated for the left hemisphere of the brain and for the tumor volume to reveal the heterogeneity of metabolic parameters between anatomical regions (mean ± 3x SD, in µmol/g).
4- The IR spectra corresponding to the anatomical regions meshed from the left hemisphere were analyzed separately (averaged spectra shown in Supplementary material 12) to reveal the mean ± SD values of metabolic parameters and plotted (12 examples provided).

Supplementary material

Supplementary materials, videos notably, are available in the online version of the paper. Reprints and permissions information is available online at www.nature.com/reprints. Correspondence and requests for materials should be addressed to C.P. cyril.petibois@u-bordeaux.fr or petibois@gate.sinica.edu.tw

Competing financial interests

The authors declare no competing financial interests.